AIMS Mathematics

https://www.aimspress.com/journal/Math

AIMS Mathematics, 10(8): 19240–19266.
DOI:10.3934/math.2025860
Received: 31 March 2025
Revised: 15 July 2025
Accepted: 21 July 2025
Published: 25 August 2025

Research article

Chaotic dynamics in Sprott's memristive artificial neural network: dynamic analysis, circuit implementation and synchronization

M. I. Kopp[1] **and I. Samuilik**[2,3,*]

[1] Institute for Single Crystals, NAS of Ukraine, Nauky Ave. 60, Kharkiv 61072, Ukraine

[2] Institute of Life Sciences and Technologies, Daugavpils University, 13 Vienibas Street, LV-5401 Daugavpils, Latvia

[3] Institute of Applied Mathematics, Riga Technical University, LV-1048 Riga, Latvia

* **Correspondence:** Email: inna.samuilika@rtu.lv.

Abstract: The paper presents a new artificial neural network (ANN) obtained by embedding a memristor into the self-connection synapse of one neuron from the Sprott ANN. The mathematical model of the new network is described by a five-dimensional (5D) dynamic system. A comprehensive analysis of its dynamic properties is carried out, including bifurcation diagrams, Lyapunov exponents, Kaplan–Yorke dimension, timing diagrams and phase portraits, multistability, and offset boosting control. The theoretical model is further verified by electronic simulation of a chaotic system using Multisim software. A synchronization model of two coupled memristive subneural Sprott networks is proposed to simulate synchronization between regions of biological neural systems. Linearization methods and Lyapunov stability theory are employed to prove synchronization. These results provide useful insights into the nonlinear dynamic characteristics of the new Sprott ANN.

Keywords: artificial neural networks (ANNs); memristor; chaotic behavior; circuit implementation; synchronization
Mathematics Subject Classification: 34A34, 37D45, 37G35, 37H15, 68T01

1. Introduction

Chaotic systems have long attracted attention due to their relevance in a wide range of fields, including nonlinear dynamics [1, 2], physics [3–5], gene networks [6, 7], neurodynamics [8], electronics [9, 10], cryptography [11], and secure communications [12]. Their sensitivity to the initial conditions and complex yet deterministic behavior make them powerful tools for modeling natural processes and designing robust artificial systems. In particular, chaos-based models have shown great promise in improving the performance and adaptability of neural networks and neuromorphic computing.

The mathematical foundations of artificial neural networks (ANNs) date back to the 1940s, with the seminal work of McCulloch and Pitts, who proposed the first mathematical model of a neuron [13]. A major milestone followed with Rosenblatt's discovery of the perceptron [14], which laid the groundwork for the development of deep neural networks (DNNs). Designed to emulate brain-like processing, ANNs have become indispensable in modern artificial intelligence, offering powerful tools for learning, pattern recognition, and decision-making in complex, high-dimensional environments [15]. Numerous biologically inspired neuron models have been proposed, including the Hindmarsh–Rose (HR) [16], FitzHugh–Nagumo (FHN) [17, 18], Hodgkin–Huxley (HH) [19, 20], and Rulkov models [21], as well as artificial systems such as the Hopfield neural network (HNN) [22].

Among these models, the HNN has garnered the most attention from researchers. Hopfield [22] was the first to develop a dynamical system with an electronic circuit implementation to model the chaotic behavior of biological nervous systems, including the human brain. This system, known as the HNN, is a fully interconnected network of n neurons and is defined as:

$$C_i \frac{dx_i}{dt} = -\frac{x_i}{R_i} + \sum_{j=1}^{n} w_{ij} \tanh x_j + I_i \, .$$

In this formulation, C_i, R_i, and x_i denote the membrane capacitance, membrane resistance, and voltage of neuron i, respectively. The $\tanh x_j$ function represents the activation function of the neuron. The synaptic weight between neurons i and j is denoted as w_{ij}, and I_i represents the external input current.

The emergence of memristors nonlinear passive circuit elements that retain memory of past states has significantly expanded the modeling capabilities of neural networks [25, 26]. Memristors exhibit a dynamic resistance that depends on the history of the current or voltage, making them ideal candidates for emulating biological synapses. When integrated into ANNs, memristors enable more biologically realistic and adaptable connectivity, allowing the design of systems with enhanced learning, memory, and signal processing abilities [27]. In recent years, memristive neural networks particularly memristive Hopfield neural networks (MHNNs) have gained substantial attention in the literature [23, 24]. These systems combine the structure of classical neural networks with the adaptive dynamics of memristors, giving rise to rich and tunable behaviors that are suitable for neuromorphic engineering, control systems, and secure communication.

Advances in computing have sparked growing interest in multidimensional networks of interacting agents, such as neurons in neural networks. With appropriate nonlinearities and interconnections, these networks can effectively model complex phenomena across the physical, social, and biological sciences. ANNs are widely utilized in various intelligent systems, including robots, self-driving cars, and more [28]. For a comprehensive review of ANNs in machine learning (ML), deep learning, and related fields, see [29]. Their applications in neuroscience and the interplay between ML and biologically realistic neuron models used for computational tasks are discussed in [30]. Additionally, the role of ANNs in pattern recognition, particularly in industrial applications, has been extensively analyzed in [31]. Furthermore, the ANN approach has been applied to the study of genetic systems, as explored in [32].

An ANN is a mathematical model that emulates the biological processes of the human brain. ANN models are typically governed by ordinary differential equations. They consist of multiple interconnected processing elements, each receiving weighted signals from multiple sources and processing them accordingly. Excitatory connections correspond to positive weights, while inhibitory connections correspond to negative weights. The incoming signals are summed linearly and then transformed by a nonlinear activation function usually a sigmoid function that regulates the output amplitude. Neural networks with arbitrary connections are commonly referred to as recurrent neural networks (RNNs). The dynamics of a continuous-time RNN are described by a system of coupled ordinary differential equations (ODEs) with a sigmoid nonlinearity of the following form [33]:

$$\frac{dx_i}{dt} = -b_i x_i + f_i\left(\sum_j w_{ij} x_j\right) + I_i,$$

where x_i represents the internal state of the i-th unit, b_i is the frictional damping parameter, w_{ij} are the connection weights, and $I_i(t)$ is the external input to the i-th unit. The response function of the i-th unit is given by $f_i\left(\sum_j w_{ij} x_j\right)$, which is typically a sigmoidal function. The main activation functions are the logistic function, hyperbolic tangent, Gaussian function, and linear function. Sigmoid response functions of the form $f_i(z) = 1/(1 + \exp(\mu_i(w_{ij} z_j - \theta_i)))$ (μ_i, θ_i are the parameters) were used in a network consisting of three neurons [34]. Similar sigmoid response functions have also been used to model genetic regulatory networks [35, 36]. Another well-known example of a network utilizing the response function $f_i(z) = \tanh(w_{ij} z_j - \theta_i)$ is described by the following set of differential equations [37]:

$$\frac{dx_i}{dt} = -b_i x_i + \tanh \sum_{j=1, j\neq i}^{N} w_{ij} x_j\,. \tag{1.1}$$

Sprott [37] found that the system (1.1), by appropriately selecting the vector b_i and the matrix w_{ij}, and with a sufficiently large N, can exhibit diverse dynamical behaviors, including chaotic regimes. As shown in [38], for a sufficiently large N, the system (1.1) can approximate any dynamical system with arbitrary precision. In [37, 39], Sprott derived several intriguing dynamical systems from system (1.1) for small values of N, which merit further investigation. Notable examples include the following [37]:

1. A minimal dissipative ANN with $N = 4$ and $b = 0.043$.
2. A minimal conservative ANN with $N = 4$ and $b = 0$.
3. A minimal circulant ANN with $N = 5$ and $b = 0.12$.

The modeling of genetic and neural networks using the dynamical system (1.1) in two-dimensional (2D) and three-dimensional (3D) cases, with weight elements differing from unity, was studied by Samuilik et al. [40, 41]. Samuilik et al. [42] expanded the study of higher-order ANN models beyond four dimensions (4D). In [42, 43], they investigated ANN models with five (5D), six (6D), and even 60 (60D) dimensions, demonstrating chaotic behavior. In this paper, we investigate a Sprott ANN comprising four neurons and an embedded memristor in the self-connecting synapse of one neuron. The unique capabilities of memristors in advancing ANN architectures motivated this study.

This manuscript is organized into several sections. The introduction provides a brief overview of the current state of the problem. Section 2 presents the derivation of a novel memristive Sprott dynamical system for an artificial neural network. In Section 3, we analyze the dynamic properties of the Sprott memristive ANN (SMANN) system by examining fixed points, constructing bifurcation diagrams, and determining both the Lyapunov exponents and Kaplan–Yorke dimension. Additionally, we explore multistability and offset boosting control within the system. Section 4 details the design of an electronic circuit implementation of the SMANN system using the Multisim environment. We validate circuit operation through simulations and compare the results with those obtained in Mathematica. Finally, Section 5 investigates synchronization in SMANN coupling, while the conclusions summarize the key findings of this study.

2. Mathematical model of a new Sprott's meristive network

The main goal of this section is to show step-by-step the derivation of the new Sprott memristive system. To implement this idea, we will first show a basic Sprott ANN, then explain the selected model of a non-ideal memristor, and finally outline how we add the memristor to the self-connection synapse of the first neuron.

Sprott's research on chaotic behavior in networks, particularly those with a large number N of agents or neurons (as in neural networks), revealed that the smallest ANN capable of exhibiting chaos can be described by four differential equations of the following form [37,39]:

$$\begin{cases} \dfrac{dx_1}{dt} = \tanh(x_4 - x_2) - bx_1, \\ \dfrac{dx_2}{dt} = \tanh(x_1 + x_4) - bx_2, \\ \dfrac{dx_3}{dt} = \tanh(x_1 + x_2 - x_4) - bx_3, \\ \dfrac{dx_4}{dt} = \tanh(x_3 - x_2) - bx_4, \end{cases} \tag{2.1}$$

where b is a parameter controlling the rate of dissipation in the system. Sprott demonstrated [37] that variations in b lead the system (2.1) to exhibit stable, periodic, and chaotic behaviors. The hyperbolic tangent function (tanh), often called a sigmoid function, ensures nonlinear saturation by bounding the output values within a finite range, thereby preventing unbounded and physically unrealistic solutions. For the parameter $b = 0.043$ and initial conditions $(x_1(0), x_2(0), x_3(0), x_4(0)) = (1.2, 0.4, 1.2, -1)$, the system exhibits a chaotic attractor. The Lyapunov exponents (LE_i, $i = 1, 2, 3, 4$) and the Kaplan–Yorke dimension D_{KY} were also determined in [37] as follows:

$$LE_i = (0.03164, 0, -0.07313, -0.13051), \quad D_{KY} = 2.43263\,. \tag{2.2}$$

Given that the system (2.1) exhibits chaotic behavior, incorporating a memristor is expected to facilitate the emergence of diverse chaotic regimes and multistability. In addition, memristors can store analog values, making them ideal for representing neural network weights. Leveraging their ability to adjust resistance on the basis of the magnitude of the electric charge, memristors can effectively model changes in the synaptic weights of neurons under external stimulation. Consequently, the use of memristors as coupled synapses is expected to play a pivotal role in the development of future neural networks.

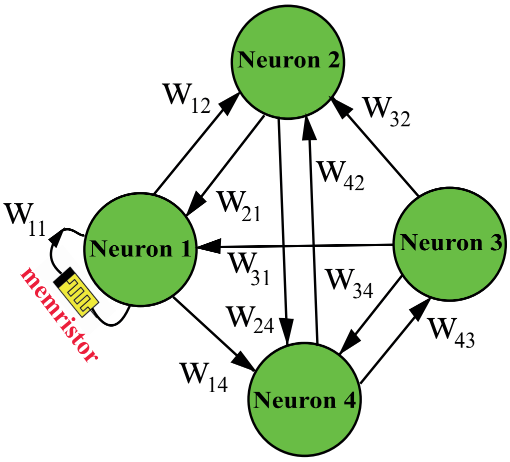

Figure 1. Connection diagram of Sprott's memristive network composed of four activation neurons. The connection weights from the i-th neuron to the j-th neuron are $w_{11} = aW(x_5), w_{12} = -1, w_{14} = 1, w_{21} = 1, w_{24} = 1, w_{31} = 1, w_{32} = 1, w_{34} = -1, w_{42} = -1$, and $w_{43} = 1$.

In this study, a memristor model with a hyperbolic tangent conductance function (see, for example, [44]) is used to emulate the self-connection synapse of Neuron 1, as illustrated in Figure 1. Additionally, Figure 1 depicts the connection structure of the neural network, which comprises four neurons. The non-ideal memristor can be expressed mathematically as:

$$\begin{cases} i_m = W(\varphi)u_m & \text{(current)}, \\ \dfrac{d\varphi}{dt} = u_m - k\varphi & \text{(flux with damping)}, \\ W(\varphi) = \tanh\varphi & \text{(memductance)}, \end{cases} \tag{2.3}$$

where i_m signifies the current flowing through the memristor, u_m denotes the voltage across the memristor, φ is the internal flux, and k is a positive parameter. The nonlinear and saturable mem-conductivity $W(\varphi) = \tanh(\varphi)$ has an S-shaped profile characterized by the following properties:

(a) Saturation: $W \to 1$ as $\varphi \to \infty$ and $W \to -1$ as $\varphi \to -\infty$;
(b) Symmetry and smoothness;
(c) Near-linear behavior around zero: $W \approx \varphi$ for small φ.

These characteristics of $W(\varphi)$ enable the emergence of hysteresis under sinusoidal excitation, impose a natural limit on conductivity (saturation behavior), and allow for rapid transitions in the system's response features that are advantageous for the generation of chaotic dynamics. The system of equations (2.3) produces nonlinear characteristic curves that pass through the origin. For the numerical modeling of this system, we apply a sinusoidal alternating voltage $u_m = A\sin(2\pi ft)$ to the memristor input, where A represents the amplitude and f the frequency of the external signal. Figure 2 shows the results of modeling the memristor system (2.3) with the flux–damping coefficient assigned a value of one: $k = 1$. When the memristor is driven by sinusoidal alternating current, its current–voltage characteristic forms a closed curve, known as the "hysteresis loop", which passes through the origin. As the amplitude A increases, the area enclosed by the hysteresis loop expands. Conversely, increasing the frequency f causes the loop area to shrink. This behavior is characteristic of memristive systems.

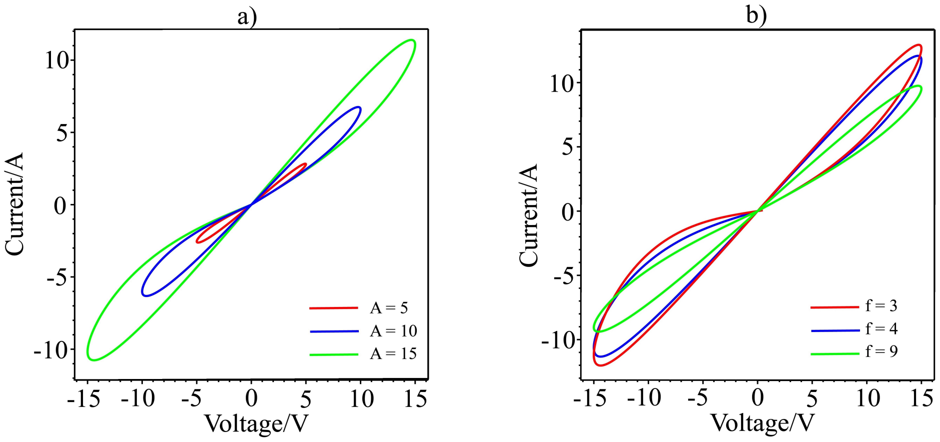

Figure 2. Simulation of the hysteresis loop of a hyperbolic tangent type memristor for: (a) different amplitude values A, (b) different values of frequency f.

By combining Eqs (2.3) and (2.1), we have derived the equations governing 5D nonlinear dynamics, which are presented in a new Sprott memristive ANN in the following form:

$$\begin{cases} \dfrac{dx_1}{dt} = \tanh(x_4 - x_2 + aW(x_5)x_1) - bx_1, \\ \dfrac{dx_2}{dt} = \tanh(x_1 + x_4) - bx_2, \\ \dfrac{dx_3}{dt} = \tanh(x_1 + x_2 - x_4) - bx_3, \\ \dfrac{dx_4}{dt} = \tanh(x_3 - x_2) - bx_4, \\ \dfrac{dx_5}{dt} = x_1 - x_5, \end{cases} \tag{2.4}$$

with the synaptic connection weight matrix defined as follows:

$$\mathbf{w} = \begin{pmatrix} aW(x_5) & -1 & 0 & 1 \\ 1 & 0 & 0 & 1 \\ 1 & 1 & 0 & -1 \\ 0 & -1 & 1 & 0 \end{pmatrix},$$

and initial conditions

$$x_1(0) = 2,\ x_2(0) = 1,\ x_3(0) = 1.5,\ x_4(0) = 0,\ x_5(0) = 2. \tag{2.5}$$

In Eq (2.4), a is the memristive coupling coefficient, which serves as a control parameter for the memristor. In addition, we replaced the flux notation φ with a new dynamic variable x_5, and the memductance $W(\varphi)$ is $W(x_5) = \tanh(x_5)$. Thus, the new Sprott memristive ANN can be controlled by two parameters, a and b. It is easy to see that the system (2.4) remains invariant under the transformation $\mathbf{T}$

$$\mathbf{T}:\ (x_1, x_2, x_3, x_4, x_5) \to (x_1, x_2, x_3, x_4, x_5).$$

To classify the system (2.4), we calculate its divergence or the trace of the matrix as follows:

$$Tr(f(x_i)) = \nabla \cdot f(x_i) = \sum_{i=1}^{5} \frac{\partial \dot{x}_i}{\partial x_i} =$$

$$-\left[(4b+1) - \frac{a\tanh(x_5)}{\cosh^2(x_4 - x_2 + a\tanh(x_5)x_1)}\right].$$

System (2.4) is dissipative for positive values in square brackets or when the following inequality is satisfied:

$$4b + 1 > \frac{a\tanh(x_5)}{\cosh^2(x_4 - x_2 + a\tanh(x_5)x_1)}.$$

The subsequent sections are dedicated to the dynamic analysis of the newly introduced system (2.4).

3. Dynamical analysis

This section considers the dynamical behaviors of the proposed SMANN using analytic and numerical analysis techniques, including bifurcation diagrams, Lyapunov exponents (LEs), phase plots, and time series.

3.1. Bifurcation diagrams, Lyapunov exponents, and Kaplan–Yorke dimension

In this section, we conduct a general analysis of the behavior of the proposed system (2.4) based on variations in the system's parameters a and b. For this purpose, we utilize tools such as bifurcation diagrams and the exponential Lyapunov spectrum (see Figures 3 and 4). Bifurcation diagrams are commonly used to graphically represent changes in the system's state variables. These diagrams provide critical insights into qualitative changes in the system's behavior as specific control parameters are varied. Lyapunov exponents (LEs) are an essential criterion for describing the behavior and stability of dynamic systems. LEs quantify the rate at which neighboring trajectories in a dynamic system diverge or converge. A dynamic system is considered to be unstable or chaotic when the largest LE is positive, while a negative LE indicates a tendency toward stable equilibrium. By examining the sign of the LEs, one can classify the system's behavior as regular, quasi-regular (e.g., 2-torus or 3-torus), chaotic, or hyperchaotic. The number of Lyapunov exponents corresponds to the dimension of the phase space of the nonlinear dynamic system. For the proposed system (2.4), there are five such indicators. In this study, the Lyapunov exponents were computed using Gram–Schmidt orthonormalization within Benettin–Wolf's algorithm [45,46], a standard and reliable approach for analyzing dynamical systems. This method ensures precise exponent estimation by iteratively linearizing the system's equations along its trajectory and tracking the divergence of nearby trajectories. To validate the methodology proposed by Binous et al. [47] and Sandri [48] in Mathematica, we calculated all the Lyapunov exponents for the Sprott system (2.1) with the initial conditions $(x_1(0), x_2(0), x_3(0), x_4(0)) = (1.2, 0.4, 1.2, -1)$ in the following form:

$$LE_1 = 0.03502, \quad LE_2 = 0.00548 \approx 0,$$
$$LE_3 = -0.08529, \quad LE_4 = -0.12721. \tag{3.1}$$

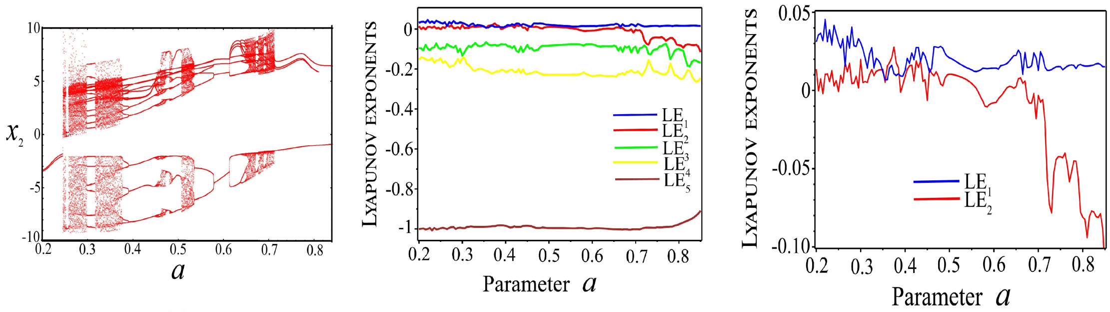

(a) (b) (c)

Figure 3. (a) Bifurcation diagram, (b) Lyapunov exponent spectra, and (c) spectra of the two largest Lyapunov exponents, all versus the memristor parameter a.

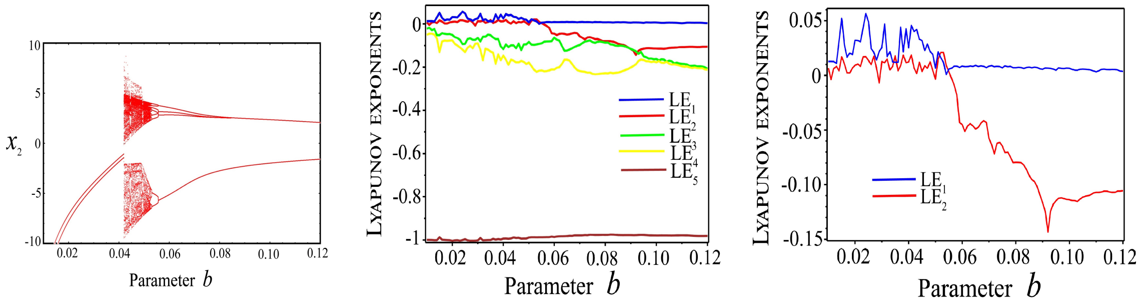

(a) (b) (c)

Figure 4. (a) Bifurcation diagram, (b) spectra of all Lyapunov exponents, and (c) spectra of the two largest Lyapunov exponents, all plotted versus the parameter b.

A comparison between the expressions (2.2) and (3.1) demonstrates strong agreement with the results of Sprott [37]. This validation allows us to confidently apply the methodology outlined in [47, 48] for calculating the Lyapunov exponents of the proposed SMANN system (2.4). Additionally, an electronic circuit implementation of the Sprott system (2.1) at $b = 0.043$ was designed and tested using the Multisim environment. Figure 5 presents the phase portrait of the chaotic attractor, as captured from the oscilloscope simulation in Multisim.

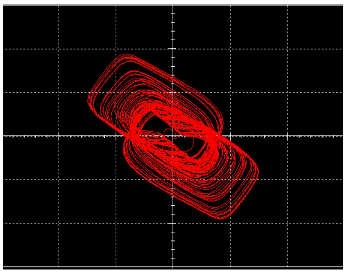

Figure 5. Phase portrait of the chaotic attractor in the Sprott system (2.1), as generated by the oscilloscope simulation in Multisim.

The two parameters a and b of system (2.4) are analyzed independently to assess their influence on the system's behavior. With the parameter $b = 0.043$ fixed and the initial conditions given in (2.5), the bifurcation diagram and the Lyapunov exponent spectrum for $a \in [0.2, 0.85]$ are presented in Figure 3.

With the parameter $a = 0.295$ being fixed and the initial conditions specified in (2.5), Figure 4 presents the bifurcation diagram and the Lyapunov exponent spectrum for when the parameter b varies within the range $b \in [0.01, 0.12]$, showcasing the system's dynamic behavior.

3.2. Analysis of equilibrium points and their stability

The equilibrium points and their stability are commonly used to uncover the generation mechanism of chaotic attractors in dynamic systems. The equilibrium points of the model (2.4) can be determined by solving the following equations:

$$\begin{cases} 0 = \tanh(\widetilde{x}_4 - \widetilde{x}_2 + a\tanh(\widetilde{x}_5)\widetilde{x}_1) - b\widetilde{x}_1, \\ 0 = \tanh(\widetilde{x}_1 + \widetilde{x}_4) - b\widetilde{x}_2, \\ 0 = \tanh(\widetilde{x}_1 + \widetilde{x}_2 - \widetilde{x}_4) - b\widetilde{x}_3, \\ 0 = \tanh(\widetilde{x}_3 - \widetilde{x}_2) - b\widetilde{x}_4, \\ 0 = \widetilde{x}_1 - \widetilde{x}_5. \end{cases} \tag{3.2}$$

The last equation of the system (2.5) gives the obvious equality $\widetilde{x}_1 = \widetilde{x}_5$. It is evident that the system (2.5) is a fourth-order transcendental equation, making its analytical solution challenging to obtain. Therefore, a numerical method is employed to determine the equilibrium points. It is possible to represent the state variables $\widetilde{x}_2$ and $\widetilde{x}_4$ as follows:

$$\widetilde{x}_2 = \frac{1}{b}\tanh(\widetilde{x}_1 + \widetilde{x}_4),\ \widetilde{x}_4 = \frac{1}{b}\tanh(\widetilde{x}_3 - \widetilde{x}_2). \tag{3.3}$$

The expression for point $\widetilde{x}_3$ can be found by substituting (3.3) into (3.2):

$$\widetilde{x}_3 = \frac{1}{b}\tanh\left(\widetilde{x}_1 - \widetilde{x}_4 + \frac{1}{b}\tanh(\widetilde{x}_1 + \widetilde{x}_4)\right). \tag{3.4}$$

Next, by substituting Eqs (3.3) and (3.4) into Eq (3.2), the equilibrium points can be determined as the intersections of the curves $F(\widetilde{x}_1, \widetilde{x}_4)$ and $G(\widetilde{x}_1, \widetilde{x}_4)$, which are expressed as follows:

$$\begin{cases} F(\widetilde{x}_1, \widetilde{x}_4) = \tanh\left(\widetilde{x}_4 - \frac{1}{b}\tanh(\widetilde{x}_1 + \widetilde{x}_4) + a\tanh(\widetilde{x}_1)\widetilde{x}_1\right) - \\ \qquad - b\widetilde{x}_1, \\ G(\widetilde{x}_1, \widetilde{x}_4) = \tanh\left(\frac{1}{b}\tanh\left(\widetilde{x}_1 - \widetilde{x}_4 + \frac{1}{b}\tanh(\widetilde{x}_1 + \widetilde{x}_4)\right) - \right. \\ \qquad \left. - \frac{1}{b}\tanh(\widetilde{x}_1 + \widetilde{x}_4)\right) - b\widetilde{x}_4. \end{cases} \tag{3.5}$$

Assuming the parameter values

$$a = 0.295, \quad b = 0.043, \tag{3.6}$$

the equilibrium points can be easily determined as the intersection points of the curves F and G. Numerical and graphical solutions of Eq (3.5), as illustrated in Figure 6, yield $\widetilde{x}_1 = 0$ and $\widetilde{x}_4 = 0$.

Substituting these into Eqs (3.3) and (3.4), we also obtain $\widetilde{x}_2 = 0$ and $\widetilde{x}_3 = 0$. Consequently, we confirm the existence of a unique equilibrium point given by $E(0, 0, 0, 0, 0)$. The stability of equilibrium points can be determined by analyzing the eigenvalues of the Jacobian matrix, whose general form is provided in the Appendix. The characteristic polynomial at the equilibrium point $E(0, 0, 0, 0, 0)$ is expressed as:

$$\lambda^5 + 1.172\lambda^4 + 3.183\lambda^3 + 2.269\lambda^2 + 0.221\lambda + 0.962 = 0. \tag{3.7}$$

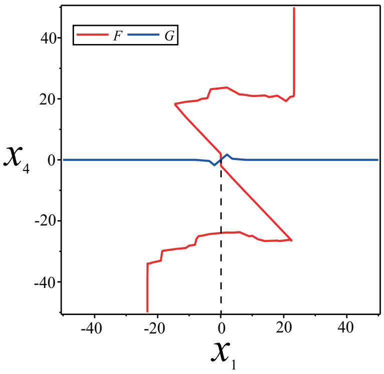

Figure 6. Function curves from (3.5) and their intersection point $(0, 0)$ are shown for a = 0.295 and b = 0.043.

We apply the Routh–Hurwitz criterion (see the Appendix) to evaluate the stability of the system in the vicinity of the fixed point E. The minors of the Hurwitz matrix corresponding to the characteristic Eq (3.7) are given as follows:

$$\Delta_1 = 1.172 > 0, \quad \Delta_2 = 1.461 > 0, \quad \Delta_3 = 4.14 > 0,$$

$$\Delta_4 = -4.40 < 0, \quad \Delta_5 = -4.23 < 0. \tag{3.8}$$

It follows that not all minors of the Hurwitz determinant are positive. As a result, the characteristic Eq (3.7) has roots with a positive real part, indicating that the system is unstable. Indeed, solving the characteristic Eq (3.7) yields the roots:

$$\lambda_1 = -1, \; \lambda_{2,3} = 0.160 \pm i0.560, \; \lambda_{4,5} = -0.246 \pm i1.663.$$

The presence of a positive real part in the complex roots $\lambda_{2,3}$ classifies the system as a saddle-focus type, indicating the instability of the system (2.4). This instability suggests that the system exhibits a self-excited attractor. Moreover, according to Shilnikov's theorem [49], chaos arises at the equilibrium point if one real root δ ($\lambda_1 = -1$) and two complex conjugate roots $\alpha + i\beta$ ($\lambda_{2,3} = 0.160 \pm i0.560$) exist satisfying

$$|\alpha/\delta| < 1 \; (|0.160/(-1)| < 1), \quad \delta\alpha < 0 \; ((-1) \cdot 0.16 < 0).$$

For the parameters values (3.6), these conditions suggest that the SMANN system generates a chaotic attractor.

The Lyapunov exponents of the new system (2.4) are numerically estimated for the parameter values given in (3.6) and the initial state specified in (2.5) as follows:

$$LE_1 = 0.03307, \; LE_2 = 0.00161 \approx 0, \; LE_3 = -0.09909,$$

$$LE_4 = -0.17036,\ LE_5 = -0.99303. \tag{3.9}$$

The presence of a positive Lyapunov exponent LE_1 confirms that the system (2.4) exhibits chaotic behavior. Furthermore, the negative sum of the Lyapunov exponents, $\sum_{i=1}^{5} LE_i = -1.228 < 0$, demonstrates that the chaotic system (2.4) is dissipative, as the energy or volume in the phase space is continuously contracted over time. The Lyapunov or Kaplan–Yorke dimension of the new chaotic system (2.4) is computed using the formula described in [50]:

$$D_{KY} = \xi + \frac{1}{|LE_{\xi+1}|} \sum_{i=1}^{\xi} LE_i = 2 + \frac{0.0346}{0.0991} \approx 2.35, \tag{3.10}$$

where ξ is determined from the conditions

$$\sum_{i=1}^{\xi} LE_i > 0 \ \Rightarrow \ \sum_{i=1}^{2} LE_i = 0.0346. \tag{3.11}$$

Here, ξ is the number of Lyapunov exponents that add up to a positive value. The Kaplan–Yorke fractional dimension offers an estimate of the fractal dimension of a strange attractor in a dynamical system, providing a quantitative measure of its complexity. Figure 7 illustrates the dynamics of the Lyapunov exponents, as defined in the expression (3.2).

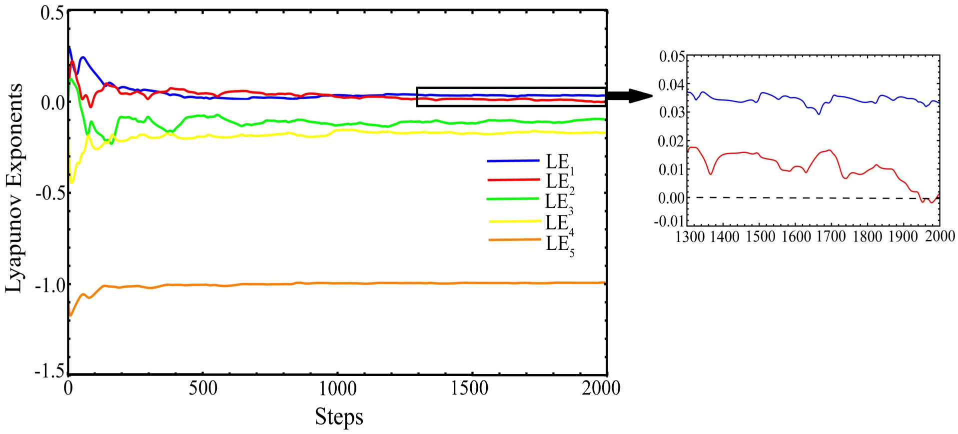

Figure 7. Convergence plot of the Lyapunov exponents for the system (2.4) at $a = 0.295$ and $b = 0.043$. The inset shows a zoomed-in view illustrating the convergence of the first two Lyapunov exponents.

3.3. *Phase portraits and sensitivity analysis*

A detailed visual analysis of the chaotic attractors is performed by using phase portraits. Using Mathematica, we plotted the phase portraits in the x_1x_2, x_1x_3, x_1x_4, and x_2x_4 planes, along with the temporal evolution of the state components for the chaotic system (2.4), as shown in Figure 8. The time series of x_1, x_2, x_3, x_4, and x_5 exhibit an aperiodic structure, a defining characteristic of chaos. As shown in Figure 8, the dynamic variables x_i remain within the operational amplifiers' power supply limits (±15 V).

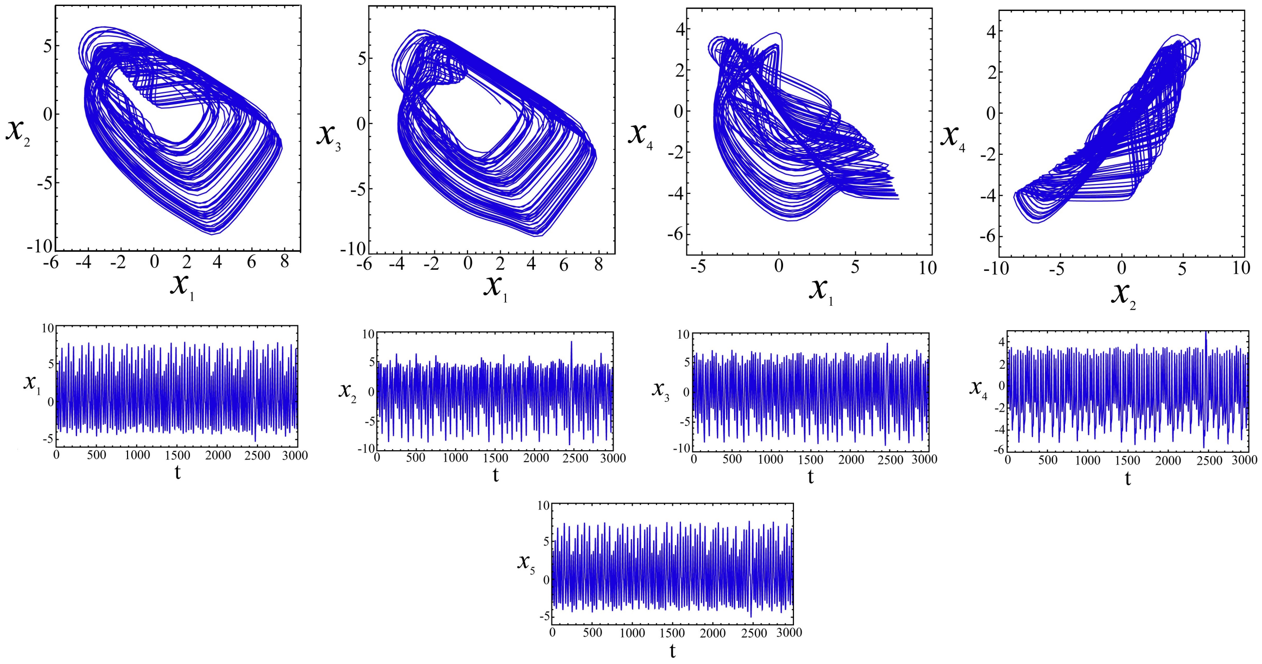

Figure 8. Chaotic attractors and temporal diagrams for the variables x_1, x_2, x_3, x_4, and x_5 of the SMANN system (2.4) with the initial conditions (2.5) and parameter values (3.6).

Sensitivity analyses of chaotic dynamic systems are essential in many engineering and scientific domains. A hallmark of chaotic behavior is its extreme sensitivity to the initial conditions, often referred to as the butterfly effect. This property implies that infinitesimal variations in initial states can lead to significantly divergent trajectories over time, making long-term predictions inherently unreliable. Figure 9 presents the trajectories of the proposed SMANN chaotic system (2.4) under two slightly different initial conditions. The trajectory corresponding to $x_1(0) = 2$ is depicted in blue, while the trajectory with a perturbed initial condition $x_1(0) = 2.0001$ is shown in red. As seen in Figure 9, the divergence of the trajectories occurs only after $t \geq 340$ s, indicating that the proposed system does not exhibit high sensitivity to the initial conditions.

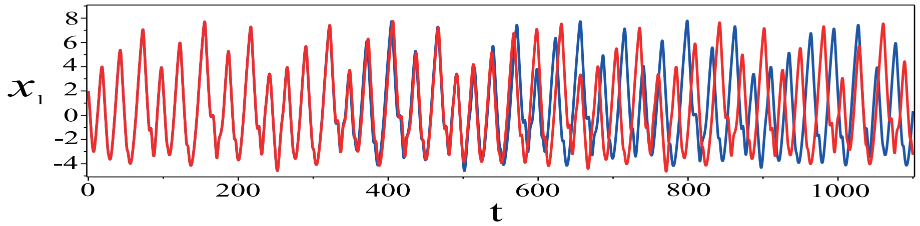

Figure 9. Illustration of the sensitivity of the SMANN chaotic system (2.4) to the initial conditions. The trajectories start from slightly different values of $x_1(0)$ and begin to diverge after $t \geq 340$ s.

3.4. *Multistability of chaotic attractors and offset boosting control*

Multistability refers to the coexistence of two or more attractors within a system for the same set of parameters, where the resulting state depends on the initial conditions. The new SMANN system (2.4) exhibits this phenomenon, demonstrating coexisting chaotic attractors under different initial conditions.

Table 1 presents data for two distinct chaotic attractors obtained by solving the system (2.4) with identical control parameters (3.6) but different initial conditions. The dynamic behavior of these attractors, as summarized in Table 1, is visually represented in Figure 10.

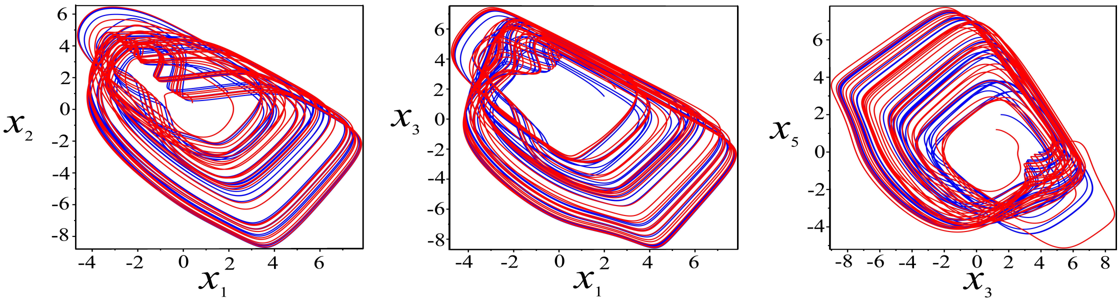

Figure 10. Plots showing the multistability of two chaotic attractors in different phase planes for the initial conditions in Table 1.

Table 1. The system (2.4) demonstrates multistability when using different initial conditions.

Figure 4 (planes)	Initial conditions	Color	Sign of *LEs*
x_1x_2	$(2, 1, 1.5, 0, 2)$	Blue	$(+, 0, -, -, -)$
x_1x_2	$(0.4, 0.395, 0.4, 0.395, 0.4)$	Red	$(+, 0, -, -, -)$
x_1x_3	$(2, 1, 1.5, 0, 2)$	Blue	$(+, 0, -, -, -)$
x_1x_3	$(2.5, 1.5, 2, 0.5, 2.5)$	Red	$(+, 0, -, -, -)$
x_3x_5	$(2, 1, 1.5, 0, 2)$	Blue	$(+, 0, -, -, -)$
x_3x_5	$(1.2, 0.4, 1.2, -1, 1.2)$	Red	$(+, 0, -, -, -)$

The offset boosting control method is a highly effective technique for manipulating chaotic systems, enabling flexible and precise shifting of the attractors in a desired direction through the introduction of an offset. This method holds significant value in engineering applications [51]. By incorporating a constant offset into specific system variables, chaotic trajectories can be systematically adjusted, facilitating controlled navigation across the phase space. We illustrate this phenomenon in the chaotic SMANN system (2.4) by introducing an offset to the state variable x_3, replacing it with $x_3 + m$, where m is a constant. As shown in Figure 11, modifying the bias gain control m effectively transforms the signal x_3 from a bipolar to a unipolar form. Adjusting m systematically shifts the attractor along the x_3-axis without altering its intrinsic structure. A comparative analysis of the three attractors reveals that their shapes and sizes remain nearly identical, differing only by a fixed translational shift in the x_3 direction.

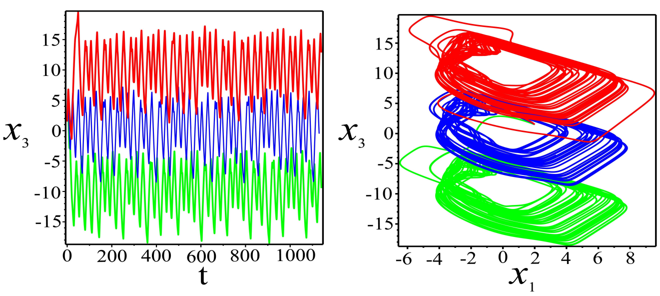

Figure 11. Signal x_3 and phase portrait in the plane x_1x_3 for different values of the offset boosting controller m: $m = 0$ (blue), $m = 10$ (green), $m = -10$ (red).

We now examine the implications of controlling the attractor shift for the state variable x_5, which is associated with the memristor. By replacing x_5 in Eq (2.4) with x_5+k, where k is a constant, we conduct a numerical simulation. The results, presented in Figure 12, reveal that, unlike the previous case, the attractor in the x_3x_5 plane undergoes a shift in both the x_3 and x_5 directions. Moreover, adjusting the bias gain parameter k effectively converts the signals x_3 and x_5 from a bipolar to a unipolar form. This demonstrates that incorporating a memristor into the ANN (2.1) allows for simultaneous control of the chaotic attractors in multiple directions.

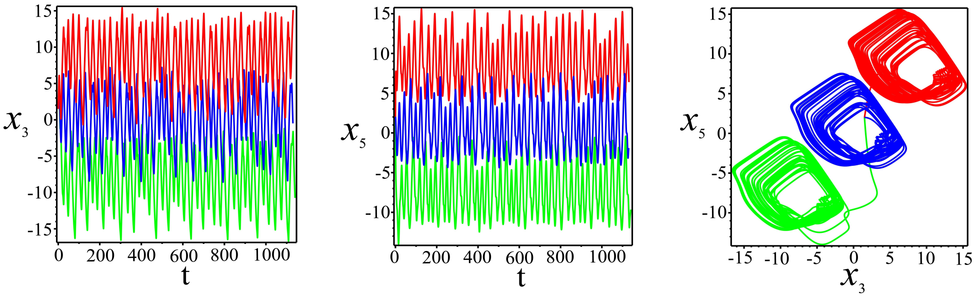

Figure 12. Signals x_3, x_5, and phase portrait in the plane x_3x_5 for different values of the offset boosting controller k: $k = 0$ (blue), $k = 8$ (green), $k = -8$ (red).

4. Circuit realization

The analog implementation of neurons and neural networks holds significant potential for practical applications in artificial intelligence devices. In this section, we design an electronic circuit to implement the proposed SMANN. The design employs an approach based on operational amplifiers and well-known electronic circuits for the hyperbolic tangent function and a memristor emulator [44]. The variables of the dynamic system (2.4) are represented by electrical signals corresponding to the instantaneous voltage values on capacitors C_1, C_2, C_3, C_4, C_5, denoted as $U_1(\tau), U_2(\tau), U_3(\tau), U_4(\tau), U_5(\tau)$, respectively.

By applying Kirchhoff's laws of the electrical circuit, the electrical analog of the system described in Eq (2.4) can be formulated as follows:

$$\begin{cases} C_1\dfrac{dU_1}{d\tau} = -\dfrac{U_1}{R_{11}} + \dfrac{1}{R_{12}}\tanh\left(U_4 - U_2 + \dfrac{U_1\tanh(U_5)}{K\cdot R_{13}}\right), \\ C_2\dfrac{dU_2}{d\tau} = -\dfrac{U_2}{R_{21}} + \dfrac{1}{R_{22}}\tanh(U_1 + U_4), \\ C_3\dfrac{dU_3}{d\tau} = -\dfrac{U_3}{R_{31}} + \dfrac{1}{R_{32}}\tanh(U_1 + U_2 - U_4), \\ C_4\dfrac{dU_4}{d\tau} = -\dfrac{U_4}{R_{41}} + \dfrac{1}{R_{42}}\tanh(U_3 - U_2), \\ C_5\dfrac{dU_5}{d\tau} = -\dfrac{U_5}{R_{51}} + \dfrac{U_1}{R_{52}}, \end{cases} \tag{4.1}$$

where R_{ij} represent resistors $(i, j) = \{1, 2, 3, 4, 5\}$, and K is a scaling coefficient for the multiplier. We normalize the resistor as $R_0 = 100\,\mathrm{k}\Omega$ and the capacitor as $C_0 = 0.15\,\mathrm{nF}$, giving a time constant of $t_0 = R_0C_0 = 1.5\cdot 10^{-5}$ s. The state variables of the system (4.1) are rescaled as follows:

$$U_1 = U_0\widetilde{X}_1, \quad U_2 = U_0\widetilde{X}_2, \quad U_3 = U_0\widetilde{X}_3, \quad U_4 = U_0\widetilde{X}_4,$$

$$U_5 = U_0\widetilde{X}_5, \quad K = U_0K^{'}, \quad \tau = t_0t.$$

By substituting R_0, $C_1 = C_2 = C_3 = C_4 = C_5 = C_0$, and $K' = 1$ into the system (4.1), and comparing the numerical values of the output voltages in (4.1) and (2.4) for the parameter values $a = 0.295$ and $b = 0.043$, we determine the values of the electronic circuit resistors as follows:

$$\begin{cases} \dfrac{d\widetilde{X}_1}{d\tau} = -\dfrac{100\mathrm{k}}{R_1}\widetilde{X}_1 + \dfrac{100\mathrm{k}}{R_2}\tanh\left(\widetilde{X}_4 - \widetilde{X}_2 + \dfrac{100\mathrm{k}}{R_3}\widetilde{X}_1\tanh(\widetilde{X}_5)\right), \\ \dfrac{d\widetilde{X}_2}{d\tau} = -\dfrac{100\mathrm{k}}{R_4}\widetilde{X}_2 + \dfrac{100\mathrm{k}}{R_5}\tanh(\widetilde{X}_1 + \widetilde{X}_4), \\ \dfrac{d\widetilde{X}_3}{d\tau} = -\dfrac{100\mathrm{k}}{R_6}\widetilde{X}_3 + \dfrac{100\mathrm{k}}{R_7}\tanh(\widetilde{X}_1 + \widetilde{X}_2 - \widetilde{X}_4), \\ \dfrac{d\widetilde{X}_4}{d\tau} = -\dfrac{100\mathrm{k}}{R_8}\widetilde{X}_4 + \dfrac{100\mathrm{k}}{R_9}\tanh(\widetilde{X}_3 - \widetilde{X}_2), \\ \dfrac{d\widetilde{X}_5}{d\tau} = -\dfrac{100\mathrm{k}}{R_{10}}\widetilde{X}_5 + \dfrac{100\mathrm{k}}{R_{11}}\widetilde{X}_1, \end{cases} \tag{4.2}$$

where

$$R_1 = R_4 = R_6 = R_8 = 2.326\mathrm{M}\Omega,$$

$$R_2 = R_5 = R_7 = R_9 = R_{10} = R_{11} = 100\mathrm{k}\Omega, \ R_3 = 338.98\mathrm{k}\Omega.$$

Figure 13 illustrates the analog circuit modules corresponding to the equations in the system (4.2). These circuits are constructed using the standard components, including resistors (R), capacitors (C), multiplier (M1, AD633), operational amplifiers (A1-A24, TL084ACN), and a supply voltage of ±15 V. Figure 14 depicts the electronic circuits for the hyperbolic tangent function and a memristor emulator. As shown in Figure 14, the equivalent circuit for the hyperbolic tangent function consists of two MPS2222 transistors (Q1 and Q2), two TL084ACN operational amplifiers, a current source

(I_0 = 1.1 mA), and several resistors. The circuit simulation results of the model are presented in Figure 15, which are consistent with the numerical simulations performed in Mathematica software (see Figure 8).

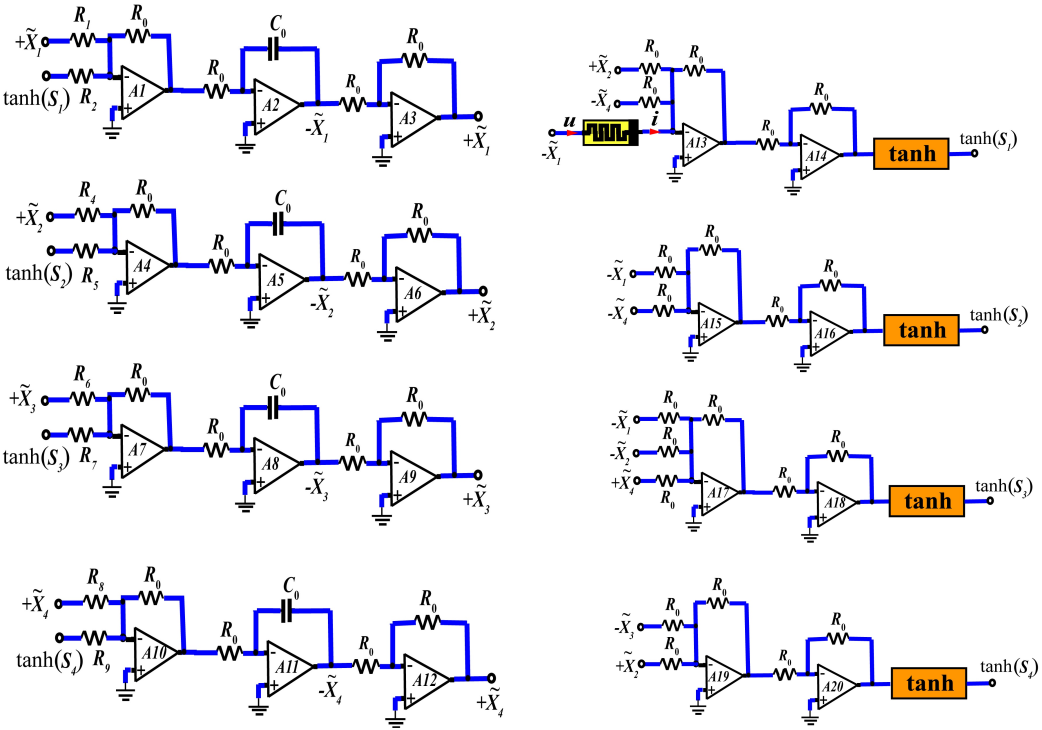

Figure 13. Circuit diagram of the SMANN system.

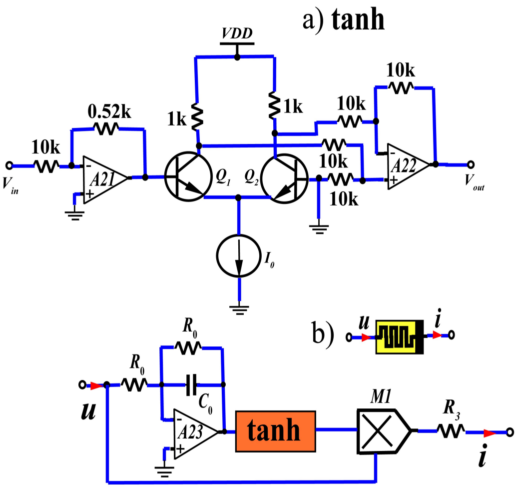

Figure 14. The circuit scheme includes two components: (a) The hyperbolic tangent function, and (b) the memristor emulator.

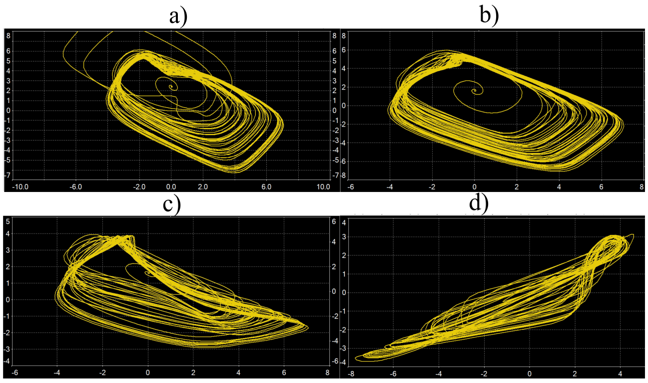

Figure 15. Phase portraits of the SMANN as generated by Multisim oscilloscopes: (a) $\widetilde{X}_1\widetilde{X}_2$; (b) $\widetilde{X}_1\widetilde{X}_3$; (c) $\widetilde{X}_1\widetilde{X}_4$; (d) $\widetilde{X}_2\widetilde{X}_4$.

5. Synchronization in the coupling SMANN

Synchronization is fundamental in ANNs, particularly those that emulate the dynamics of biological neural systems. In the brain, electrical activity plays a crucial role in synchronizing specific regions, enabling efficient information transfer. This is achieved through interregional neural networks, where neurons establish synaptic connections to facilitate communication. In this context, we investigate the synchronization of two subnetworks implemented using a small neural network (SMANN) based on Eq (3). These subnetworks are interconnected through a synaptic link via a single neuron. Let $(x_1, x_2, x_3, x_4, x_5)$ and $(y_1, y_2, y_3, y_4, y_5)$ denote the state variables of the first and second subnetworks, respectively. The corresponding synaptic coupling model of SMANN is formulated as follows:

$$\begin{cases} \dfrac{dx_1}{dt} = \tanh(x_4 - x_2 + aW(x_5)x_1) - bx_1 + p(x_1 - y_1), \\ \dfrac{dx_2}{dt} = \tanh(x_1 + x_4) - bx_2, \\ \dfrac{dx_3}{dt} = \tanh(x_1 + x_2 - x_4) - bx_3, \\ \dfrac{dx_4}{dt} = \tanh(x_3 - x_2) - bx_4, \\ \dfrac{dx_5}{dt} = x_1 - x_5, \\ \dfrac{dy_1}{dt} = \tanh(y_4 - y_2 + aW(y_5)y_1) - by_1 - p(x_1 - y_1), \\ \dfrac{dy_2}{dt} = \tanh(y_1 + y_4) - by_2, \\ \dfrac{dy_3}{dt} = \tanh(y_1 + y_2 - y_4) - by_3, \\ \dfrac{dy_4}{dt} = \tanh(y_3 - y_2) - by_4, \\ \dfrac{dy_5}{dt} = y_1 - y_5, \end{cases} \tag{5.1}$$

where p represents the synaptic coupling strength of the sub-neural networks. To illustrate the synchronization process, we present the following algorithmic framework.

Algorithm 1: Synchronization of two coupled sub-neural networks

```
Input: Initial states $\mathbf{x}(0)$, $\mathbf{y}(0)$; parameters $a$, $b$, $p$; step $\Delta t$; final time $T$
Output: Trajectories $\mathbf{x}(t)$, $\mathbf{y}(t)$; synchronization error $E(t)$
for $t = 0$ to $T$ step $\Delta t$ do                                  // time loop
    Compute master system derivatives:;
    $\dot{x}_1 = \tanh(x_4 - x_2 + aW(x_5)x_1) - bx_1 + p(x_1 - y_1)$;
    $\dot{x}_2 = \tanh(x_1 + x_4) - bx_2$;
    $\dot{x}_3 = \tanh(x_1 + x_2 - x_4) - bx_3$;
    $\dot{x}_4 = \tanh(x_3 - x_2) - bx_4$;
    $\dot{x}_5 = x_1 - x_5$;
    Compute slave system derivatives:;
    $\dot{y}_1 = \tanh(y_4 - y_2 + aW(y_5)y_1) - by_1 - p(x_1 - y_1)$;
    $\dot{y}_2 = \tanh(y_1 + y_4) - by_2$;
    $\dot{y}_3 = \tanh(y_1 + y_2 - y_4) - by_3$;
    $\dot{y}_4 = \tanh(y_3 - y_2) - by_4$;
    $\dot{y}_5 = y_1 - y_5$;
    Integrate both systems (e.g., RK4);
    Compute error $E(t) = \|x_1 - y_1\|$;
```

5.1. Stability of synchronous states

The stability of synchronous states in coupled neural networks is a fundamental aspect of their dynamical behavior. The complete synchronization of the coupled neural network in Eq (5.1) is achieved when the two subnetworks asymptotically converge to identical dynamical behavior. Mathematically, this implies that as $t \to \infty$,

$$\lim_{t\to\infty} e_i = \lim_{t\to\infty}(x_i - y_i) = 0, \quad i = (1,2,3,4,5), \tag{5.2}$$

where e_i is the synchronization error. According to the Eq (5.2), the system in Eq (5.1) gives rise to the following error dynamics system:

$$\begin{cases} \dfrac{de_1}{dt} = \tanh(x_4 - x_2 + aW(x_5)x_1) - \tanh(y_4 - y_2 + aW(y_5)y_1) - \\ \qquad - be_1 + 2p\,e_1, \\ \dfrac{de_2}{dt} = \tanh(x_1 + x_4) - \tanh(y_1 + y_4) - e_2, \\ \dfrac{de_3}{dt} = \tanh(x_1 + x_2 - x_4) - \tanh(y_1 + y_2 - y_4) - be_3, \\ \dfrac{de_4}{dt} = \tanh(x_3 - x_2) - \tanh(y_3 - y_2) - be_4, \\ \dfrac{de_5}{dt} = e_1 - e_5. \end{cases} \tag{5.3}$$

The synchronization problem between the two subnetworks reduces to ensuring that the error dynamics governed by Eq (5.3) are asymptotically stable. To achieve this, we derive the characteristic equation and compute the corresponding eigenvalues for the system (5.3), expressed as follows:

$$\begin{gathered}(\lambda + b - 2p)(\lambda + b)^3(\lambda + 1) = 0,\\ \lambda_1 = -1, \lambda_2 = -b + 2p, \lambda_3 = -b, \lambda_4 = -b, \lambda_5 = -b.\end{gathered} \tag{5.4}$$

The error system (5.3) is asymptotically stable if all its eigenvalues have negative real parts. This stability condition is satisfied if the following criteria are met:

$$b > 0, \quad -b + 2p < 0. \tag{5.5}$$

Another approach to analyzing stability is based on the Lyapunov stability criterion. We construct a continuous, positive-definite Lyapunov function of the following form:

$$V = \frac{1}{2}\left(e_1^2 + e_2^2 + e_3^2 + e_4^2 + e_5^2\right). \tag{5.6}$$

The time derivative of the Lyapunov function V, evaluated along the trajectories of the error dynamical system (5.3), is given by

$$\frac{dV}{dt} = (2p - b)e_1^2 - b(e_2^2 + e_3^2 + e_4^2) + e_1e_5 - e_5^2 + h, \tag{5.7}$$

where h is a function defined as

$$\begin{gathered}h = e_1(\tanh(x_4 - x_2 + aW(x_5)x_1) - \tanh(y_4 - y_2 + aW(y_5)y_1))+\\ +e_2(\tanh(x_1 + x_4) - \tanh(y_1 + y_4))+\\ +e_3(\tanh(x_1 + x_2 - x_4) - \tanh(y_1 + y_2 - y_4))+\\ +e_4(\tanh(x_3 - x_2) - \tanh(y_3 - y_2)).\end{gathered}$$

For all $x_i \in \mathbb{R}$, where $\tanh(x_i) < 1$ and $\tanh(x_i) \in (-1, 1)$, the upper bound of the function h can be estimated as:

$$h \leq 2(|e_1| + |e_2| + |e_3| + |e_4|). \tag{5.8}$$

As result, putting (5.8) into (5.7), we have

$$\begin{gathered}\frac{dV}{dt} = (2p - b)e_1^2 - b(e_2^2 + e_3^2 + e_4^2) + e_1e_5 - e_5^2 + h \leq (2p - b)e_1^2 -\\ -b(e_2^2 + e_3^2 + e_4^2) + e_1e_5 - e_5^2 + 2(|e_1| + |e_2| + |e_3| + |e_4|).\end{gathered} \tag{5.9}$$

To achieve asymptotic stability, it is necessary and sufficient that dV/dt is negative semidefinite. Since the two sub-neural networks have bounded trajectories, a sufficiently large constant C exists. For all state variables satisfying

$$\begin{gathered}x_1 - y_1 = e_1 < C,\ x_2 - y_2 = e_2 < C,\ x_3 - y_3 = e_3 < C,\\ x_4 - y_4 = e_4 < C,\ x_5 - y_5 = e_5 < C,\end{gathered}$$

it follows that:

$$\frac{dV}{dt} \leq (2p - b)C^2 - 3bC^2 + 8|C| < 0. \tag{5.10}$$

Therefore, when $2p - b < 0, b > 0$ holds, Eq (5.10) is ultimately uniformly bounded.

5.2. Numerical simulation results

In this subsection, to numerically verify synchronization in the coupled SMANN system, we utilized the nonlinear Eqs (5.1) and (5.3), applying the fourth- and fifth- order Runge–Kutta–Fehlberg (*rkf*45) method in the Maple computing environment. We use the fixed control parameters (3.6) and the initial conditions (ICs) for the two subnetworks as follows:

$$\begin{gathered}(x_1(0), x_2(0), x_3(0), x_4(0), x_5(0)) = \\ = (2.0001, 1.0001, 1.5001, 0.0001, 2.0001), \\ (y_1(0), y_2(0), y_3(0), y_4(0), y_5(0)) = (2, 1, 1.5, 0, 2). \qquad (5.11)\end{gathered}$$

For a coupling strength of $p = -0.2$, the simulation results are presented in Figures 16–17. Figure 16 illustrates the time evolution of the potentials on Neuron 1 in both subnetworks, demonstrating that they coincide very well. Figure 17 shows that after coupling the two SMANNs, the difference between the potentials of corresponding neurons rapidly decreases to nearly zero. This behavior indicates complete synchronization, where the distance between the states of the two coupled systems approaches zero at $t \to \infty$, i.e., the synchronization error $e_i \to 0$.

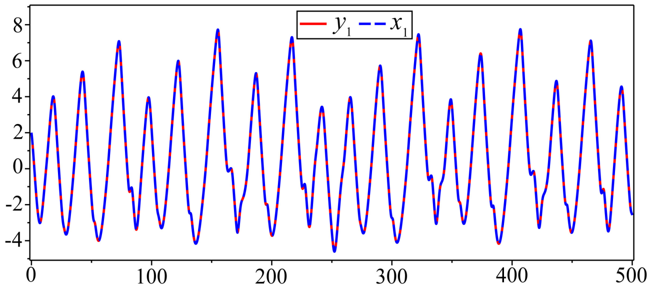

Figure 16. Time diagram of signals (x_1, y_1) of two subnetworks of Neuron 1.

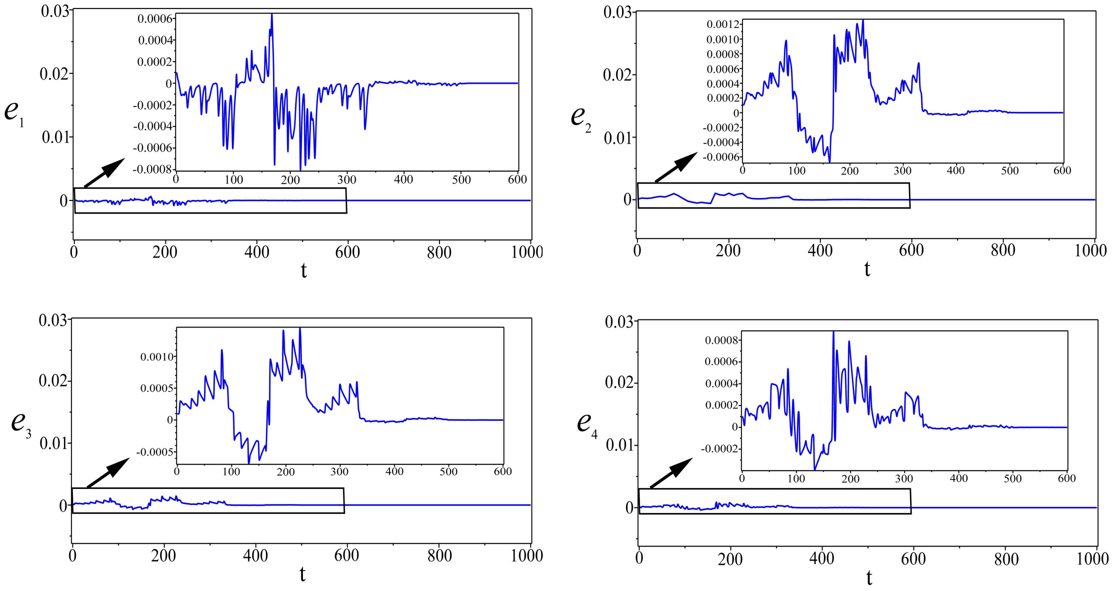

Figure 17. Errors synchronization of subnetworks over time.

Generalized synchronization provides flexible coordination between coupled subsystems without requiring identical trajectories, making it suitable for structurally non-identical or memristive networks. Its main advantage is robustness to parameter mismatch and functional variability. However, it lacks explicit convergence time bounds and may lead to increased transient energy consumption. Compared with fixed-time and finite-time synchronization, which guarantee synchronization within known time intervals and can be optimized for energy efficiency, generalized synchronization is less predictable in its timing and energy use. In contrast to Kuramoto oscillator networks, which are simple and energy-efficient for phase synchronization, the proposed model enables more complex coupling but at a higher computational and energy cost. Recent approaches involving fractional-order multilayer networks allow for better prediction and optimization of energy consumption. While generalized synchronization offers structural adaptability, it may not match the predictability and control efficiency of these more advanced schemes.

6. Conclusions

In this study, we introduced and analyzed a novel 5D ANN based on the Sprott system, augmented with a memristor (referred to as SMANN), where the memristor emulates the self-feedback of the first neuron. By employing a memristor with a hyperbolic tangent conductance function, the network gains an additional layer of nonlinearity and flexibility, significantly enriching its dynamics. A detailed investigation of the system's behavior was performed through bifurcation analysis, Lyapunov spectra, phase portraits, and the study of multistability. The results demonstrate that the inclusion of a memristive element enables more effective control over the system's dynamics. In particular, varying the memristor parameter allows the modulation of the system's behavior across a much broader range compared with the control parameter of the original Sprott ANN. This highlights the memristor's potential as a powerful tool for fine-tuning and controlling complex neural dynamics. Moreover, the system exhibits offset boosting behavior that preserves the sign of the Lyapunov exponents, confirming the robustness of its chaotic regime under external modulation. The proposed dual-SMANN synchronization framework also opens avenues for modeling interbrain communication, with asymptotic stability rigorously established via linearization and Lyapunov stability theory. The proposed method, based on generalized synchronization, demonstrates high robustness to structural and parametric mismatches, making it suitable for complex and heterogeneous neural systems. However, the lack of explicit convergence time and energy efficiency optimization remains a limitation. Future work may focus on integrating time-constrained or energy-aware synchronization schemes, extending the approach to fractional-order or multilayer networks, and exploring its application to real-time control and neuromorphic systems.

Overall, the integration of a memristor into the neural network architecture not only enhances the dimensionality and complexity of the system but also substantially improves its controllability, making it a promising candidate for advanced neuromorphic modeling. Future research will focus on implementing the proposed memristive Sprott ANN in both analog and digital hardware. Additionally, we aim to explore potential applications of this chaotic system in secure communications, the Internet of Things (IoT), and other emerging technologies.

Author contributions

M. I. Kopp: conceptualization, methodology, software, validation, formal analysis, investigation, data curation, writing-original draft preparation, writing-review and editing, visualization, supervision; I. Samuilik: conceptualization, validation, investigation, resources, writing-original draft preparation, writing-review and editing, visualization, supervision. All authors have read and approved the final version of the manuscript for publication.

Use of Generative-AI tools declaration

The authors declare they has not used Artificial Intelligence (AI) tools in the creation of this article.

Acknowledgments

The authors gratefully acknowledge the anonymous reviewers for their valuable feedback, which helped improve the manuscript.

Conflict of interest

The authors declare no conflicts of interest.

References

1. A. A. Shukur, V.-T. Pham, V. K. Tamba, G. Grassi, Hyperchaotic oscillator with line and spherical equilibria: stability, entropy, and implementation for random number generation, *Symmetry*, **16** (2024), 1341. https://doi.org/10.3390/sym16101341
2. Z. Li, S. Zhao, Bifurcation, chaotic behavior and solitary wave solutions for the Akbota equation, *AIMS Mathematics*, **9** (2024), 22590–22601. https://doi.org/10.3934/math.20241100
3. K. Zhang, J. P. Cao, Dynamic behavior and modulation instability of the generalized coupled fractional nonlinear Helmholtz equation with cubic-quintic term, *Open Phys.*, **23** (2025), 20250144. https://doi.org/10.1515/phys-2025-0144
4. T. Bohr, M. H. Jensen, G. Paladin, A. Vulpiani, *Dynamical systems approach to turbulence*, 2 Eds., Cambridge: Cambridge University Press, 2009. https://doi.org/10.1017/CBO9780511599972
5. S. Soldatenko, A. Bogomolov, A. Ronzhin, Mathematical modelling of climate change and variability in the context of outdoor ergonomics, *Mathematics*, **9** (2021), 2920. https://doi.org/10.3390/math9222920
6. O. Kozlovska, F. Sadyrbaev, I. Samuilik, A new 3D chaotic attractor in gene regulatory network, *Mathematics*, **12** (2024), 100. https://doi.org/10.3390/math12010100
7. J. Demongeot, F. Sadyrbaev, I. Samuilik, Mathematical modeling of gene networks, *Front. Appl. Math. Stat.*, **10** (2024), 1514380. https://doi.org/10.3389/fams.2024.1514380

8. X. X. Yin, J. Chen, W. X. Yu, Y. Huang, W. X. Wei, X. J. Xiang, et al., Five-dimensional memristive Hopfield neural network dynamics analysis and its application in secure communication, *Circuit World*, **50** (2024), 67–81. https://doi.org/10.1108/cw-05-2022-0135
9. A. Ipatovs, I. C. Victor, D. Pikulins, S. Tjukovs, A. Litvinenko, Complete bifurcation analysis of the vilnius chaotic oscillator, *Electronics*, **12** (2023), 2861. https://doi.org/10.3390/electronics12132861
10. S. Tjukovs, D. Surmacs, J. Grizans, C. V. Iheanacho, D. Pikulins, Implementation of buck DC-DC converter as built-in chaos generator for secure IoT, *Electronics*, **13** (2024), 20. https://doi.org/10.3390/electronics13010020
11. S. Hashemi, M. A. Pourmina, S. Mobayen, M. R. Alagheband, Multiuser wireless speech encryption using synchronized chaotic systems, *Int. J. Speech. Technol.*, **24** (2021), 651–663. https://doi.org/10.1007/s10772-021-09821-3
12. K. U. Shahna, Novel chaos based cryptosystem using four-dimensional hyper chaotic map with efficient permutation and substitution techniques, *Chaos Soliton. Fract.*, **170** (2023), 113383. https://doi.org/10.1016/j.chaos.2023.113383
13. I. N. da Silva, D. H. Spatti, R. A. Flauzino, L. H. Bartocci Liboni, S. F. dos Reis Alves, *Artificial neural networks: A practical course*, Cham: Springer, 2017. https://doi.org/10.1007/978-3-319-43162-8
14. M. Minsky, S. A. Papert, *Perceptrons: An introduction to computational geometry*, Cambridge: The MIT Press, 2017. https://doi.org/10.7551/mitpress/11301.001.0001
15. A. Baliyan, K. Gaurav, S. K. Mishra, A review of short term load forecasting using artificial neural network models, *Procedia Computer Science*, **48** (2015), 121–125. https://doi.org/10.1016/j.procs.2015.04.160
16. J. L. Hindmarsh, R. M. Rose, A model of the nerve impulse using two first-order differential equations, *Nature*, **296** (1982), 162–164. https://doi.org/10.1038/296162a0
17. R. FitzHugh, Impulses and physiological states in theoretical models of nerve membrane, *Biophys. J.*, **1** (1961), 445–466. https://doi.org/10.1016/S0006-3495(61)86902-6
18. J. Nagumo, S. Arimoto, S. Yoshizawa, An Active pulse transmission line simulating nerve axon, *Proceedings of the IRE*, **50** (1962), 2061–2070. https://doi.org/10.1109/JRPROC.1962.288235
19. A. L. Hodgkin, A. F. Huxley, A quantitative description of membrane current and its application to conduction and excitation in nerve, *J. Physiol.*, **117** (1952), 500–544. https://doi.org/10.1113/jphysiol.1952.sp004764
20. Z. T. Njitacke, S. Parthasarathy, C. N. Takembo, K. Rajagopal, J. Awrejcewicz, Dynamics of a memristive FitzHugh-Rinzel neuron model: application to information patterns, *Eur. Phys. J. Plus*, **138** (2023), 473. https://doi.org/10.1140/epjp/s13360-023-04120-z
21. C. X. Wang, H. J. Cao, Parameter space of the Rulkov chaotic neuron model, *Commun. Nonlinear Sci.*, **19** (2014), 2060–2070. https://doi.org/10.1016/j.cnsns.2013.10.004
22. J. J. Hopfield, Neurons with graded response have collective computational properties like those of two-state neurons, *Proc. Natl. Acad. Sci. U.S.A.*, **81** (1984), 3088–3092. https://doi.org/10.1073/pnas.81.10.3088

23. H. R. Lin, C. H. Wang, Q. L. Deng, C. Xu, Z. K. Deng, C. Zhou, Review on chaotic dynamics of memristive neuron and neural network, *Nonlinear Dyn.*, **106** (2021), 959–973. https://doi.org/10.1007/s11071-021-06853-x
24. H. R. Lin, C. H. Wang, F. Yu, J. R. Sun, S. C. Du, Z. K. Deng, et al., A review of chaotic systems based On memristive hopfield neural networks, *Mathematics*, **11** (2023), 1369. https://doi.org/10.3390/math11061369
25. L. Chua, Memristor-The missing circuit element, *IEEE Transactions on Circuit Theory*, **18** (1971), 507–519. http://doi.org/10.1109/TCT.1971.1083337
26. D. B. Strukov, G. S. Snider, D. R. Stewart, R. S. Williams, The missing memristor found, *Nature*, **453** (2008), 80–83. http://doi.org/10.1038/nature06932
27. Y. C. Huang, J. X. Liu, J. Harkin, L. McDaid, Y. L. Luo, An memristor-based synapse implementation using BCM learning rule, *Neurocomputing*, **423** (2021), 336–342. https://doi.org/10.1016/j.neucom.2020.10.106
28. B. W. Yan, G. J. Wang, J. G. Yu, X. Z. Jin, H. L. Zhang, Spatial-temporal Chebyshev graph neural network for traffic flow prediction in IoT-based ITS, *IEEE Internet Things*, **9** (2022), 9266–9279. https://doi.org/10.1109/JIOT.2021.3105446
29. L. Alzubaidi, J. L. Zhang, A. J. Humaidi, A. Al-Dujaili, Y. Duan, O. Al-Shamma, et al., Review of deep learning: Concepts, CNN architectures, challenges, applications, future directions, *J. Big Data*, **8** (2021), 53. https://doi.org/10.1186/s40537-021-00444-8
30. K. Yamazaki, V. K. Vo-Ho, B. Darshan, N. Le, Spiking neural networks and their applications: A review, *Brain Sci.*, **12** (2022), 863. https://doi.org/10.3390/brainsci12070863
31. O. I. Abiodun, A. Jantan, A. E. Omolara, K. V. Dada, A. M. Umar, et al., Comprehensive review of artificial neural network applications to pattern recognition, *IEEE Access*, **7** (2019), 158820–158846. https://doi.org/10.1109/ACCESS.2019.2945545
32. J. Vohradsky, Neural network model of gene expression, *FASEB J.*, **15** (2001), 846–854. https://doi.org/10.1096/fj.00-0361com
33. S. Haykin, *Neural networks: A comprehensive foundation*, New Jersey: Prentice-Hall, 1998.
34. A. Das, A. B. Roy, P. Das, Chaos in a three dimensional neural network, *Appl. Math. Model.*, **24** (2000), 511–522. https://doi.org/10.1016/S0307-904X(99)00046-3
35. O. Kozlovska, F. Sadyrbaev, On attractors in systems of ordinary differential equations arising in models of genetic networks, *Vibroengineering PROCEDIA*, **49** (2023), 136–140. https://doi.org/10.21595/vp.2023.23343
36. O. Kozlovska, F. Sadyrbaev, I. Samuilik, A new 3D chaotic attractor in gene regulatory network, *Mathematics*, **12** (2024), 100. https://doi.org/10.3390/math12010100
37. J. C. Sprott, Chaotic dynamics on large networks, *Chaos*, **18** (2008), 023135. https://doi.org/10.1063/1.2945229
38. K. Funahashi, Y. Nakamura, Approximation of dynamical systems by continuous time recurrent neural networks, *Neural Networks*, **6** (1993), 801–806. https://doi.org/10.1016/s0893-6080(05)80125-x

39. J. C. Sprott, *Elegant chaos algebraically simple chaotic flows*, Singapore: World Scientific Publishing Company, 2010. https://doi.org/10.1142/7183
40. I. Samuilik, F. Sadyrbaev, D. Ogorelova, Comparative analysis of models of gene and neural networks, *Contemp. Math.*, **4** (2023), 217–229. https://doi.org/10.37256/cm.4220232404
41. D. Ogorelova, F. Sadyrbaev, Remarks on the mathematical modeling of gene and neuronal networks by ordinary differential equations, *Axioms*, **13** (2024), 61. https://doi.org/10.3390/axioms13010061
42. I. Samuilik, F. Sadyrbaev, S. Atslega, On mathematical models of artificial neural networks, *The 22nd International Scientific Conference "Engineering for Rural Development"*, Latvija, Jelgava, 2023, 45–50.
43. I. Samuilik, A mathematical model for a class of networks in applications, Phd Thesis, Daugavpils University, 2023.
44. Q. L. Deng, C. H. Wang, H. R. Lin, Memristive Hopfield neural network dynamics with heterogeneous activation functions and its application, *Chaos Soliton. Fract.*, **178** (2024), 114387. https://doi.org/10.1016/j.chaos.2023.114387
45. G. Benettin, L. Galgani, A. Giorgilli, J.-M. Strelcyn, Lyapunov characteristic exponents for smooth dynamical systems and for hamiltonian systems: A method for computing all of them, *Meccanica*, **15** (1980), 9–20. https://doi.org/10.1007/BF02128236
46. A. Wolf, J. B. Swift, H. L. Swinney, J. A. Vastano, Determining Lyapunov exponents from a time series, *Physica D*, **16** (1985), 285–317. https://doi.org/10.1016/0167-2789(85)90011-9
47. H. Binous, N. Zakia, *An improved method for Lyapunov exponents computation*, Wolfram Library Archive, 2008. Available from: https://library.wolfram.com/infocenter/ID/7109/ .
48. M. Sandri, Numerical calculation of Lyapunov exponents, *The Mathematica Journal*, **6** (1996), 78–84.
49. C. P. Silva, Shil'nikov's theorem: A tutorial, *IEEE T. Circuits*, **40** (1993), 675–682. https://doi.org/10.1109/81.246142
50. P. Frederickson, J. L. Kaplan, E. D. Yorke, J. A. Yorke, The Liapunov dimension of strange attractors, *J. Differ. Equations*, **49** (1983), 185–207. https://doi.org/10.1016/0022-0396(83)90011-6
51. J. J. Wen, Y. R. Feng, X. H. Tao, Y. H. Cao, Dynamical analysis of a new chaotic system: Hidden attractor, coexisting-attractors, offset boosting, and DSP realization, *IEEE Access*, **9** (2021), 167920–167927. https://doi.org/10.1109/ACCESS.2021.3136249
52. E. W. Weisstein, *Routh-Hurwitz theorem*, MathWorld: A wolfram web resource. Available from: `https://mathworld.wolfram.com/Routh-HurwitzTheorem.html`.

Appendix. The equation of the characteristic polynomial and the Routh-Hurwitz stability criterion

The classification of fixed points is performed by analyzing the behavior of trajectories in a small neighborhood around these points. To achieve this, we consider small deviations $x_i^{'}$ (perturbations) from the coordinates of the fixed points $\widetilde{x_i}$. Retaining only the linear terms, the system of Eq (2.4) reduces to the following form for the following perturbations:

$$\begin{cases} \dfrac{dx_1'}{dt} = g_1 x_4' - g_1 x_2' + g_1^{(1)} x_1' + g_1^{(2)} x_5' - b x_1', \\ \dfrac{dx_2'}{dt} = g_2 x_1' + g_2 x_4' - b x_2', \\ \dfrac{dx_3'}{dt} = g_3 x_1' + g_3 x_2' - g_3 x_4' - b x_3', \\ \dfrac{dx_4'}{dt} = g_4 x_3' - g_4 x_2' - b x_4', \\ \dfrac{dx_5'}{dt} = x_1' - x_5', \end{cases} \tag{6.1}$$

where

$$g_1 = \frac{4\mathrm{e}^{-2(\widetilde{x_4} - \widetilde{x_2} + a\tanh(\widetilde{x_5})\widetilde{x_1})}}{(1 + \mathrm{e}^{-2(\widetilde{x_4} - \widetilde{x_2} + a\tanh(\widetilde{x_5})\widetilde{x_1})})^2}, \ g_1^{(1)} = a g_1 \tanh(\widetilde{x_5}),$$

$$g_1^{(2)} = \frac{a g_1 \widetilde{x_1}}{\cosh^2(\widetilde{x_5})}, \ g_2 = \frac{4\mathrm{e}^{-2(\widetilde{x_1} + \widetilde{x_4})}}{(1 + \mathrm{e}^{-2(\widetilde{x_1} + \widetilde{x_4})})^2},$$

$$g_3 = \frac{4\mathrm{e}^{-2(\widetilde{x_1} + \widetilde{x_2} - \widetilde{x_4})}}{(1 + \mathrm{e}^{-2(\widetilde{x_1} + \widetilde{x_2} - \widetilde{x_4})})^2}, \ g_4 = \frac{4\mathrm{e}^{-2(\widetilde{x_3} - \widetilde{x_2})}}{(1 + \mathrm{e}^{-2(\widetilde{x_3} - \widetilde{x_2})})^2}.$$

Equation (6.1) can be written in a compact form through the Jacobian matrix as follows:

$$\mathbf{M} = J(E)\mathbf{N},$$

$$\mathbf{M} = \left(\frac{dx_1'}{dt}, \frac{dx_2'}{dt}, \frac{dx_3'}{dt}, \frac{dx_4'}{dt}, \frac{dx_5'}{dt} \right)^T,$$

$$\mathbf{N} = (x_1', x_2', x_3', x_4', x_5')^T, \tag{6.2}$$

where $J(E)$ is the Jacobian matrix evaluated at the fixed points:

$$J(E) = \begin{vmatrix} -b + g_1^{(1)} & -g_1 & 0 & g_1 & g_1^{(2)} \\ g_2 & -b & 0 & g_2 & 0 \\ g_3 & g_3 & -b & -g_3 & \\ 0 & -g_4 & g_4 & -b & 0 \\ 1 & 0 & 0 & 0 & -1 \end{vmatrix}. \tag{6.3}$$

Particular solutions of the system of Eq (6.2) with constant coefficients are sought in the following form:

$$x_i'(t) = x_{0i}' e^{\lambda t}, \tag{6.4}$$

where λ is the eigenvalue to be determined. Substituting Eq (6.4) into Eq (6.3), we derive the characteristic equation for the eigenvalues of the Jacobian matrix

$$\det(J - \lambda I) = 0, \tag{6.5}$$

where I is the identity matrix. By expanding the determinant (6.5), the characteristic equation is obtained in the form of a fifth-degree polynomial in λ:

$$P(\lambda) \equiv a_0\lambda^5 + a_1\lambda^4 + a_2\lambda^3 + a_3\lambda^2 + a_4\lambda + a_5 = 0, \tag{6.6}$$

where

$$\begin{gathered}
a_0 = 1,\ a_1 = 4b - g_1^{(1)} + 1,\ a_2 = 6b^2 + 4b - g_1^{(2)} - g_1^{(1)}(3b+1)+ \\
+g_2(g_1 + g_4) + g_3g_4,\ a_3 = 4b^3 + 3b^2(2 - g_1^{(1)}) - 3b(g_1^{(1)}+ \\
+g_1^{(2)}) + g_2(g_1 + g_4)(1 + 2b) + g_3g_4(1 + 2b - g_1^{(1)} - g_1 - g_2)+ \\
+g_2g_4(g_1 - g_1^{(1)}),\ a_4 = b^4 + b^3(4 - g_1^{(1)})+ \\
+(b^2 + 2b)(g_1g_2 + g_4(g_2 + g_3)) - (g_1^{(1)} + g_1^{(2)})(3b^2 + g_3g_4)+ \\
+bg_4(g_2(g_1 - g_1^{(1)}) - g_3(g_1 + g_2 + g_1^{(1)})) + g_2g_3g_4(g_1 + g_1^{(1)})+ \\
+g_4(g_1(g_2 - g_3) - g_2(g_1^{(1)} + g_1^{(2)} + g_3)),\ a_5 = b^4 - b^3(g_1^{(1)} + g_1^{(2)})+ \\
+b^2(g_2(g_1 + g_4) + g_3g_4) - b(g_2g_4(g_1^{(1)} + g_1^{(2)} - g_1) + g_1g_3g_4)+ \\
+g_3g_4((g_1^{(1)} + g_1^{(2)})(g_2 - b) + g_2(g_1 - b)).
\end{gathered}$$

According to [52], for the system to be stable, it is necessary and sufficient that all minors of the Hurwitz determinant

$$\Delta_5 = \begin{vmatrix} a_1 & a_3 & a_5 & 0 & 0 \\ a_0 & a_2 & a_4 & 0 & 0 \\ 0 & a_1 & a_3 & a_5 & 0 \\ 0 & a_0 & a_2 & a_4 & 0 \\ 0 & 0 & a_1 & a_3 & a_5 \end{vmatrix}$$

are positive:

$$\begin{gathered}
\Delta_1 = a_1 > 0, \quad \Delta_2 = a_1a_2 - a_0a_3 > 0, \\
\Delta_3 = a_3\Delta_2 - a_1(a_1a_4 - a_0a_5) > 0, \\
\Delta_4 = a_4\Delta_3 - a_5(a_2\Delta_2 - a_0(a_1a_4 - a_1a_5)) > 0,\ \Delta_5 = a_5\Delta_4 > 0.
\end{gathered} \tag{6.7}$$

AIMS Press